View metadata, citation and similar papers at core.ac.uk
brought to you by CORE
provided by Infoscience - École polytechnique fédérale de Lausanne

High Spatial Resolution of Thin-Film-on-ASIC Particle Detectors

Andrea Franco, Yannick Riesen, Matthieu Despeisse, Nicolas Wyrsch, and Christophe Ballif

***Abstract*—Thin-film-on-ASIC (TFA) detectors are monolithic pixel devices that consist of amorphous silicon detecting diodes directly deposited on readout electronics.**

This paper presents a characterization of the TFA spatial resolution using the electron-beam-induced current (EBIC) technique, in which pixel pads patterned in microstrips were swept by the beam. We measured the spatial resolution for different configurations and thicknesses of the TFA active layer with different beam energies, currents and sweep speeds. We observed that the generated electron-hole pairs are collected most efficiently when the beam is over the microstrips. This better collection efficiency gives a larger signal than off the strips, and thereby enabled us to distinguish strips as small as 0.6 μm wide which are spaced by 1.4 μm gaps.

This high spatial resolution was obtained even though microvoids in the amorphous silicon layer—induced by an ASIC morphology as rough as 2 μm—were observed in the detector cross section, thus demonstrating the potential of the TFA architecture even with non-planar readout electronics.

***Index Terms*—Amorphous silicon, ASIC, EBIC, electron interaction, particle detectors, pixel.**

I. Introduction

CRYSTALLINE silicon microstrip detectors are well-established technologies for particle tracking in high-energy physics [1]. Pixel detectors made of crystalline silicon are widely used in a number of fields from particle physics to biology and medicine [2], [3]. However mature the technology, the next upgrade of the Large Hadron Collider (LHC) and the interest in alternative detectors have fostered research and development of more radiation-hard materials [4], novel concepts [5] and detectors with enhanced temporal and spatial resolution [2]. In this context, thin-film-on-ASIC (TFA) pixel detectors were realized through a collaboration between CERN and the Institute of Microengineering in Neuchâtel [6], [7]. Within this project the TFA, originally developed for visible light imagers [8], was applied for the first time to particle detection. The sensing element is made of a hydrogenated amorphous silicon (a-Si:H) diode with a thick intrinsic active layer and thin doped layers. The diode is directly deposited on top of few different ASICs for signal amplification at the front-end.

Manuscript received February 22, 2012; revised May 31, 2012; accepted July 06, 2012. Date of publication September 10, 2012; date of current version October 09, 2012. This work was supported by the Swiss National Science Foundation under Contract 200021_126926/1.

The authors are with the Ecole Polytechnique Fédérale de Lausanne (EPFL), Institute of Microengineering (IMT), Photovoltaics and Thin-Film Electronics Laboratory, Breguet 2, CH-2000 Neuchâtel, Switzerland (e-mail: andrea.franco@epfl.ch).

Digital Object Identifier 10.1109/TNS.2012.2208478

This vertical integration scheme offers a number of advantages. First, it eliminates the complicated and expensive bump bonding technique. Indeed, a-Si:H can be deposited from the gas phase by plasma-enhanced chemical vapor deposition (PECVD) at relatively low temperatures on a variety of substrate geometries [6], [9]. This permits one to attain an active area of close to 100% (without guard rings). Furthermore, the sensing layer and the electronics can be independently developed and optimized. Finally, compared to standard pixel detectors, the TFA is more compact and potentially cheaper.

The choice of a-Si:H for the detector sensing layer is motivated by its high radiation hardness with respect to displacement damage [17], [18]. Its disordered structure and hydrogen content (10%–20%), used to passivate electronic defects and limit degradation of the material properties. As an example, a-Si:H-based detectors were demonstrated to retain reasonable performance (a loss of only 50% in the proton-induced current) after irradiation with a 24 GeV proton beam with a fluence of up to $2 \cdot 10^{16}$ cm^{-2}[19]. This fluence corresponds to five years of operation of the future Super LHC (SLHC) and explains the presence of a-Si:H on a list of candidate materials for SHLC next-generation detectors [4]. A larger degradation is observed when irradiating with charged particles of low and medium energies (tens to hundreds of keV) as all of their energy is transferred to the material [19]–[22]. This is the case for the measurements with the electron beam presented in this paper. Degradation in a-Si:H is due to the creation of metastable mid-gap states from electron-hole recombination events, and leads to a reduction of the lifetime without affecting carrier mobility. These radiation-induced defects can be removed by heating the material at temperatures between 120 and 200°C for a few hours.

a-Si:H has a band gap of 1.8 eV, which results in lower thermal noise compared to crystalline silicon, but has an increased electron-hole creation energy of 4.8 ± 1.4 eV [10]–[12]. Its electronic properties are inferior to those of crystalline silicon due to its disordered structure, which results in the presence of localized states in the band gap in the form of band tails and mid-gap states (with a density of 10^{16} cm^{-3}). As a consequence, the drift mobility is about 1 $\mathrm{cm}^2 \cdot \mathrm{V}^{-1} \cdot \mathrm{s}^{-1}$ for electrons and as low as $3 \cdot 10^{-3}$ $\mathrm{cm}^2 \cdot \mathrm{V}^{-1} \cdot \mathrm{s}^{-1}$ for holes [9], [13], [14]. Furthermore, in transient experiments, the holes do not contribute to the detector signal. The high band gap and low mobility lead to a high resistivity of the intrinsic material of 10^{11}–10^{12} $\Omega \cdot \mathrm{cm}$. Charge recombination takes place at mid-gap states with lifetimes of 1 μs[15]. Diffusion coefficients are on the order of 10^{-2}–10^{-3} $\mathrm{cm}^2 \cdot \mathrm{s}^{-1}$ for electrons and 10^{-4}–10^{-3} $\mathrm{cm}^2 \cdot \mathrm{s}^{-1}$ for holes [16]. It follows that, in TFA, charge diffusion can be neglected and high electric fields are

0018-9499/$31.00 © 2012 IEEE

required to collect charges via drift with minimum recombination.

State-of-the-art a-Si:H active layers have thicknesses of a few tens of micrometers [23] in contrast to much thicker crystalline silicon detectors. The thickness is limited by leakage currents, which are induced by the large bias voltages needed to fully deplete the intrinsic layer, and which eventually become intolerable for the ASIC [11]. As a consequence the detection of individual minimum ionizing particles (MIPs) becomes a challenge with about 1500 electrons collected in a 30-μm-thick active layer [2].

The TFA measured in the present work was initially aimed at investigating the technology potential for detecting different particle types and energies as well as studying the influence of pixel design on the device performance. It was characterized with a 660 nm pulsed laser [24], which revealed the difficulty of fully depleting a 32 μm thick a-Si:H layer while avoiding high leakage currents. The measurements also pointed out the remarkable speed of TFA with a signal formation of 18 ns at the front-end amplifier. Additionally, tests conducted with 5.9 keV X-rays [11] and MIPs [18] highlighted the importance of having active layers thicker than 15 μm for their individual detection.

The potential of TFA regarding high spatial resolution was demonstrated when detecting beta particles with very low crosstalk for strips 6.6 μm wide separated by 3.4 μm gaps [11].

These promising results called for a more detailed analysis of TFA spatial resolution for tracking applications. For this purpose, new tests with electron beams of medium energies (few tens of keV) were conducted on a number of ASIC pixels, whose metallization had been patterned in micrometric strips. The results are presented in this paper and confirm the high spatial resolution potential of the TFA down to the micrometer range.

II. Samples

The TFA structure for particle detection has been thoroughly described in previous works [6], [11]. The detecting element is made of a-Si:H, deposited on top of an ASIC as shown in Fig. 1. a-Si:H deposition was done at the Institute of Microengineering (IMT), in Neuchâtel, by PE-CVD at 70 MHz and $200^{\circ}\mathrm{C}$. The precursor gases were silane and hydrogen with a silane concentration (relative to the total gas flow) of 77%. The detecting element consists of a diode featuring a p-doped layer as thin as 30 nm, a thick intrinsic active layer which corresponds approximately to the total diode thickness, and a thin n-doped layer of about 30 nm (Fig. 1). Diodes with 5, 10 and 20 μm thick active layers were deposited and measured. The resistivity of this intrinsic layer ranged from 10^{11}–$10^{12}\ \Omega\cdot\mathrm{cm}$, whereas that of the doped layers varied from 10^{3}–$10^{5}\ \Omega\cdot\mathrm{cm}$. The p-layer and especially the p/i interface were optimized to reduce leakage currents. The n-layer plays an important role in determining spatial resolution as discussed hereafter. The bias voltage was applied by means of a gold pad glued onto a 200 nm thick transparent conductive oxide (TCO) layer, which was deposited on the p-layer. The TCO acts as a common top electrode for the sensing layer, whereas the bottom electrode is segmented and corresponds to the ASIC pixels. Additionally, an alternative configuration called M-i-p was tested. "M" stands here for metal, meaning that the n-layer is absent and the intrinsic layer

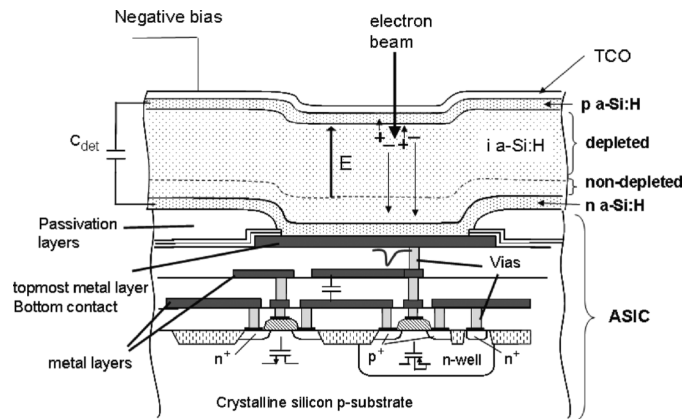

Fig. 1. Detector cross section showing the TCO top electrode, the a-Si:H n-i-p diode and one ASIC pixel pad which acts as a bottom electrode and is connected to the amplification circuit.

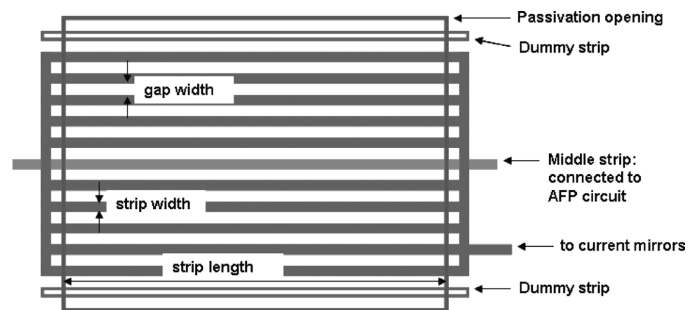

Fig. 2. Layout of the tested pixel pads, patterned in many microstrips, connected by two lateral strips. Exceptions are the middle strip, connected to an AFP circuit, and the two outermost floating strips.

is in direct contact with the bottom electrode. The advantage of the M-i-p configuration is lower leakage currents, especially for relatively thin diodes [25], but its influence on spatial resolution had not been investigated before this work.

The ASIC used in this work, as well as the detector itself, is called "aSiHtest" from the ASIC code name. It was designed in an IBM 0.25 μm CMOS technology at CERN and has three levels of metallization separated by insulating layers. The topmost metal layer is patterned in 45 pixels, each of which acts as an independent bottom electrode and defines the shape and size of a specific active area [11]. The "aSiHtest" provides two types of signal amplifiers which are connected to different pixels. The first, not used in the present study, is a current-sensitive preamplifier, called active feedback preamplifier (AFP) [26]. The second is simply made of three stages of current mirrors which provide a tunable current amplification of 10^{2}–10^{5}.

Electron-beam-induced current (EBIC) measurements were carried out on a number of ASIC pixels, which were patterned in microstrips of different lengths and widths (listed in Table I). As shown in Fig. 2, the microstrips are connected by means of two lateral strips. Exceptions are the middle strip, connected to an AFP and not measured, and the outermost strips which are dummies, i.e., floating strips.

III. Setup

The electron beam was provided by a Philips XL 30 FEG environmental scanning electron microscope (ESEM). Different

TABLE I
CHARACTERISTICS OF THE STRIP PATTERNING FOR THE TESTED PIXELS

Number of strips	Length (μm)	Strip width (μm)	Gap width (μm)	Pitch (μm)
43	767	0.6	1.4	2
23	621.3	1.5	3.5	5
13	282	6.6	13.4	20
13	113	16.5	33.5	50

sets of beam parameters were chosen according to simulation results obtained with the Monte Carlo software CASINO v2.42 [27] in order to achieve different penetration depths, lateral charge spreading and total absorbed doses. The beam currents were 40, 200, and 350 pA, and the electron energies were 10, 15, and 20 keV.

The interactions of the electron beam with the TFA were imaged with EBIC [28]. In this technique, the sample is swept by the electron beam while in short-circuit or a biased condition (reverse bias for the TFA). A map is generated in which brighter areas correspond to more efficient charge collection. Consequently the map provides qualitative access to the electric field distribution inside the device.

EBIC maps were processed with a KE 31 Current Amplifier, by KE Developments Limited (KED), together with a SEM video board. The induced current for individual beam sweeps was measured with a Tektronix TDS2012 oscilloscope.

IV. RESULTS AND DISCUSSION

A. Electric Field Profile in TFA and Lateral Charge Collection (LCC) Parameter

As mentioned in the introduction, charge diffusion can be neglected in a-Si:H. Therefore, it is important to have an electric field in the intrinsic layer to collect via drift the generated charges and limit their recombination. When the a-Si:H diode is not fully depleted, a portion of the intrinsic layer is without electric field, and the maximum attainable TFA signal is reduced as observed in a previous work [11]. The internal electric field profile in a-Si:H p-i-n diodes under reverse bias is controlled by the ionized mid-gap states, and has been extensively described elsewhere [7], [13], [29]. To simplify its analytical derivation, the common approximations of linear electric field versus depth and constant ionized defect concentration are adopted [29]:

$$E(x) = \frac{qN_{db}^*}{\varepsilon_0\varepsilon_{aSi}}(W-x) = \sqrt{\frac{2qN_{db}^*}{\varepsilon_0\varepsilon_{aSi}}V_F} - \frac{qN_{db}^*}{\varepsilon_0\varepsilon_{aSi}}\cdot x \quad (1)$$

with

$$V_F = \frac{qN_{db}^* W^2}{2\varepsilon_0\varepsilon_{aSi}} \quad (2)$$

where q is the elementary charge, N_{db}^* is the density of positively ionized defects, ε_0 is the vacuum permittivity, ε_{aSi} is the permittivity of a-Si:H, W is the depleted thickness which in this case corresponds to intrinsic layer thickness, and V_F is the bias required to fully deplete the intrinsic layer.

Previous measurements identified a minimum required reverse bias of 180 V to fully deplete an intrinsic layer of 20 μm [11]. This bias corresponds to an average electric field of $9\cdot 10^4\ \mathrm{V\cdot cm^{-1}}$, which was adopted in the present work for all

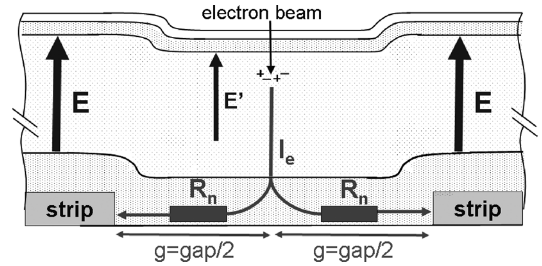

Fig. 3. Schematic representation of the current path (I_e) with the lowest resistivity, and the weakened electric field (E') due to the voltage drop in the n-layer, which reduces charge collection between strips.

intrinsic layer thicknesses. This resulted in bias voltages which exceeded V_F for the 5 and 10 μm thick intrinsic layers due to the square dependency of (2) on W. As mentioned in the introduction, energy transferred to the material by ionization indirectly produces additional defects through recombination events. The resulting ionized defects renders the electric field profile steeper according to (1), larger at the p/i interface, and weaker at the i/n interface. The field at the i/n interface decreases more and more for thicker active layers and vanishes for the 20 μm thick layer and the selected bias voltage. Further increasing the bias was not an option here, as the leakage currents above 180 V were near the acceptable limit of the detector itself. The effects on charge collection are presented in Section IV-E.

Besides measurement-induced ionized defects, the electric field is further weakened when the beam is between two strips. As shown in Fig. 3, for a beam between two strips, the generated electrons have to move not only vertically but also laterally to be collected by the adjacent strips. Their movement towards the connected strips follows the electric field gradient and the path with lowest resistivity, which means that the electrons first drift downwards through the intrinsic layer ($\rho = 10^{11}\ \Omega\cdot\mathrm{cm}$) and then laterally transferred through the n-layer ($\rho = 10^4\ \Omega\cdot\mathrm{cm}$). Although the n-layer has a resistivity seven orders of magnitude lower than the intrinsic layer, the electron flow through this thin layer (30 nm) creates a voltage drop proportional to the distance from the nearest strips. This voltage drop, in turn, decreases the difference in potential across the diode together with the electric field strength (E' in Fig. 3). As a result, charge collection efficiency decreases. The resulting signal drop can then be used to determine the beam position. In contrast to crystalline silicon microstrip detectors, in which the charge sharing mechanism is exploited, position is determined in TFA microstrips by charge recombination (due to field reduction).

In the M-i-p configuration, the lack of n-layer hinders the spreading of the strip potential at the bottom of the active layer so that the electric field between strips is weaker even before the measurements. This reduces charge collection and creates a current modulation similar to the n-i-p configuration one.

The signal variation has been quantified with the lateral charge collection (*LCC*) parameter, defined as

$$LCC\,(\%) = \frac{I_{betstrips} - I_{leak}}{I_{strip} - I_{leak}}\cdot 100 \quad (3)$$

where I_{strip} is the average current when the beam is on a strip, $I_{betstrips}$ is the average current when the beam is between any

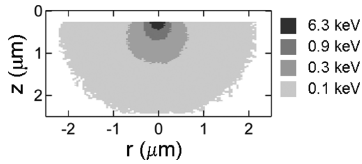

Fig. 4. Simulated map of the energy deposited at different depths and lateral spreads from the beam axis inside the TFA active layer for a 15 keV electron beam. The difference between the beam (15 keV) and deposited energy in the active layer (7.6 keV, calculated as the sum of the energies deposited in the regions of different grayscale tonalities) is given by the energy lost in the TCO and p-layer plus the backscattered electron energy.

two strips (at equal distance), and I_{leak} is the leakage current without the beam. Ideally, an *LCC* value of 50% between strips would be optimal for clearly determining the beam position, on one hand, and not losing too much charge on the other. However, the spatial resolution of the TFA microstrips can be empirically defined as the closest strip geometry which still exhibits a signal modulation of at least three times the noise, for a given particle beam. The results of lateral charge collection and spatial resolution with few microstrip geometries are presented in Sections IV-D and IV-E for different electron beams and active layer thicknesses, respectively. A comparison of *LCC* results obtained on M-i-p and n-i-p devices is given and discussed in Section IV-F.

B. Beam Interaction and Degradation in a-Si:H

The ionizing energy released by the electron beam in TFA, in terms of electron-hole generation rate and volume, was assessed by means of Monte Carlo simulations [27]. The software simulates electron interactions on user-defined 1D samples with energies typically employed in microscopy (1 to 30 keV) and outputs a 3D matrix of deposited energy in the material. As shown in Fig. 4, for a TFA active layer, the interaction volume is droplet-shaped with most of the energy released close to the beam focus point. The regions of different grayscale tonalities indicate how much energy is deposited in the active layer at different depths and lateral spreads from the beam axis. The energy deposited in the TCO and p-doped layers is not taken into account here. The elastic electron scattering at large angles produces an important lateral spread which is defined as the diameter of the disk containing 95% of the released energy. In Section IV-D, the influence of the lateral spread on the measured TFA spatial resolution is discussed.

The simulation results for the electron beam energies and currents adopted for this work are reported in Table II. The interaction between the beam and active layer was found to be confined within 3 $\mu\mathrm{m}$ in depth for the highest energy of 20 keV, confirming that the electrons release all of their energy in the active layer.

First experimental beam sweeps at 15 keV and 350 pA, with a speed of 8 $\mu\mathrm{m}\cdot\mathrm{s}^{-1}$ along 150 $\mu\mathrm{m}$, produced an absorbed dose of 31 MGy within 735 $\mu\mathrm{m}^3$. To minimize this degradation, a compromise was made between the beam sweep speed and the oscilloscope sampling rate, which resulted in a sweep speed of 680 $\mu\mathrm{m}\cdot\mathrm{s}^{-1}$. Although the dose was reduced to 360 kGy, the degradation still caused the induced current to decrease by 18% at each sweep on the same line. Sweeps at 10 keV and 40 pA allowed us to reduce the dose to 104 kGy within a volume of 75 $\mu\mathrm{m}^3$. However, the beam energy could not be reduced below 10 keV because the signal became comparable to the noise level. The beam current of 40 pA was already the lowest possible provided by the microscope.

TABLE II
SIMULATED ELECTRON BEAM ENERGIES AND CURRENTS ALONG WITH THE RELEVANT RESULTS OF INTERACTION VOLUME AND GENERATION RATE

Beam energy (keV)	Beam current (pA)	Interaction volume (μm^3)	Lateral spread (μm)	Generation rate (10^{22} cm^3·s)
10	40	1	1.0	8.5
10	200	1	1.0	44
15	350	22	2.8	13
20	350	121	4.3	4

As mentioned in the introduction, the degradation of a-Si:H, caused by EBIC measurements, consists in the creation of additional mid-gap defects. As discussed before, these additional defects increase recombination and reduce the electric field extension across the intrinsic layer, according to (1). Additionally, the a-Si:H diode leakage current (J_{th}) depends on the number of defects, according to [30]

$$J_{th} = q \cdot d \cdot N_{db} \cdot \frac{1}{\tau_{gen}} e^{\wedge} \left(\frac{-(E_C - E_t)}{kT} \right) \quad (4)$$

where q is the electron charge, d is the is the intrinsic layer thickness, N_{db} is the defect density, τ_{gen} is the time constant for charges thermal generation, and E_c and E_t are the bottom of the conduction band and the trap energy level, respectively. In conclusion, the degradation results in a drop of the signal-to-noise ratio on account of enhanced recombination, weaker electric field near the i/n interface and higher leakage currents.

Nevertheless, the mid-gap defects in a-Si:H are metastable which means that their concentration can be brought back to pre-degradation values by annealing at temperatures up to the deposition temperature ($\leq 200^\circ\mathrm{C}$) [19], [22]. The "aSiHtest" detector with the 10 $\mu\mathrm{m}$ thick intrinsic layer, which absorbed a dose of about 17.6 MGy (in 2250 $\mu\mathrm{m}^3$) for each sweep, recovered 70% of its initial signal-to-noise ratio after 70 hours of annealing at $130^\circ\mathrm{C}$. Higher annealing temperatures were not adopted because they exceed the maximum ratings of the interface board to which "aSiHtest" was bonded.

C. EBIC Maps and Line Measurements

Fig. 5 shows an EBIC map of the pixel with 13.4 $\mu\mathrm{m}$ gap width and 5 $\mu\mathrm{m}$ thick intrinsic layer obtained with a beam current of 350 pA and an energy of 15 keV. The brightest signal is recorded when the beam is focused on each connected strip, meaning that charges generated at these regions are collected most efficiently. The small black dots of Fig. 5 are caused by hillocks 1 to 5 $\mu\mathrm{m}$ wide, formed by less-dense a-Si:H agglomerates embedded during deposition. These agglomerates have a high density of defects which act as recombination centers and make the induced current drop to a similar level as between two strips.

Fig. 6 exhibits the measured induced current for a single line sweep across half of the connected strips with the same beam

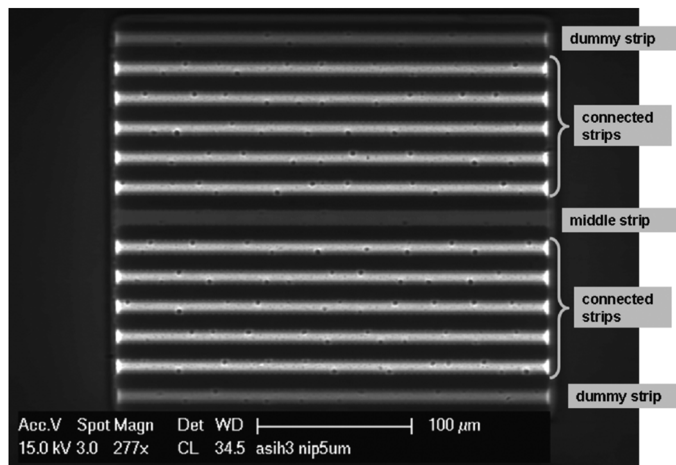

Fig. 5. EBIC map for strips spaced by 13.4 μm with an intrinsic layer of 5 μm and electron beam parameters of 15 keV and 340 pA.

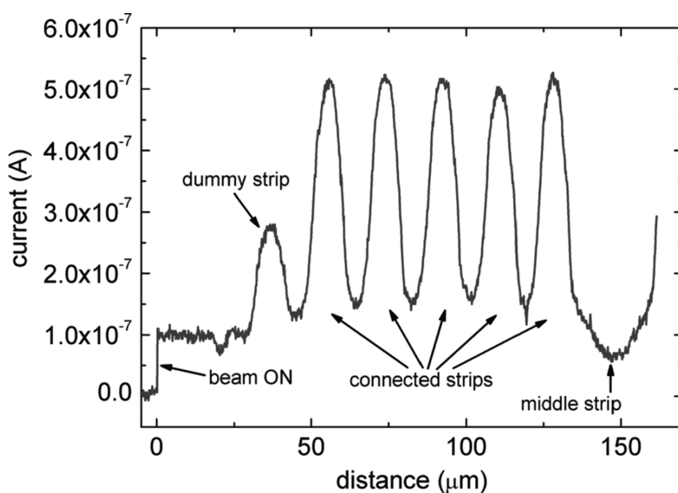

Fig. 6. Line scan of the induced current used to build the EBIC map of Fig. 5. Here the beam swept across half of the connected strips.

parameters as for Fig. 5. As observed in the EBIC map, the current reaches a maximum when the beam is above a strip. Between two strips, the induced current is reduced by two-thirds due to electric field weakening, as explained in Section IV-A.

The dummy strips exhibit a signal about half that of the other strips. The electrons that reach the aluminum metallization of the dummy strip first spread on its entire surface and then move laterally to be collected by the adjacent connected strip. As a consequence, the equivalent resistance for transfer through the n-layer is lower than that for electrons deposited between two strips due to a much larger cross-sectional area. The voltage drop stays lower accordingly, and the charge collection is more efficient than between strips, as shown in Fig. 6.

The middle strip is another particular case. In Fig. 6, its signal at $\mathrm{x} = 150\ \mu\mathrm{m}$ stays even lower than that measured at $\mathrm{x} = 0\ \mu\mathrm{m}$, when the beam is switched on outside the pixel on the ASIC passivation layer. The middle strip is connected to an AFP, and when not powered, this AFP can be modeled with a resistor going to ground. When the beam is upon the middle strip, the electrons are split between the nearest connected strips and

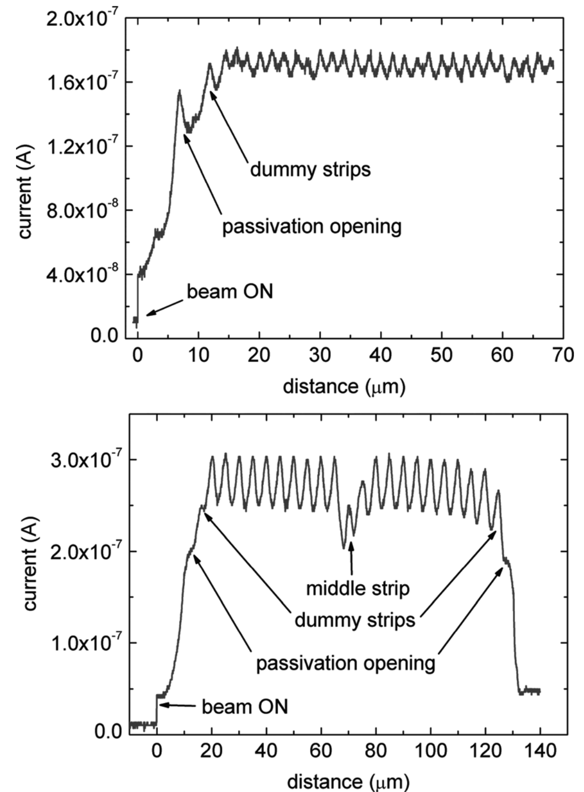

Fig. 7. Induced current for 10 μm thick active layer on strips spaced by 1.4 μm (top) and 3.5 μm (bottom) swept by a 10 keV and 200 pA electron beam.

the AFP circuit, with a ratio equal to the n-layer internal resistance over the AFP internal resistance. Now, the lowest current of Fig. 6 is in apparent contradiction to the EBIC map of Fig. 5, where the middle strip has slightly brighter signal than between two strips. The explanation is the much faster scan speed—and hence smaller charge generation—of EBIC maps compared to individual sweeps. The AFP modeled resistance has a value that depends on the current flowing through it, and it becomes more resistive for lower generation rates. As a result, proportionally more current is collected by the adjacent connected strips and the EBIC signal stays higher.

The current modulation shown in Fig. 6 is expected to attenuate for closer strips because the voltage drop in the n-layer becomes less important. Fig. 7 shows the induced current for a 10 keV and 200 pA beam upon two patterned pixels with the 10 μm thick active layer. The strip gaps are 1.4 μm for Fig. 7 (top) and 3.5 μm for Fig. 7 (bottom). The beam energy was chosen, according to the simulation results, to have the smallest lateral spread, on the one hand, and enough charge to provide a representative signal on the other. However, especially for the strips 1.4 μm apart, the dampening of the current modulation is partly caused by the lateral spread of the interaction volume, whose width becomes comparable to the strip gap and causes non-negligible collection by both strips. Despite this limitation, the current modulations of Fig. 7 allow the clear distinction of each strip, even for strips 0.6 μm wide and 1.4 μm apart. These results confirm the high TFA spatial resolution when detecting electrons of medium energy (tens of keV).

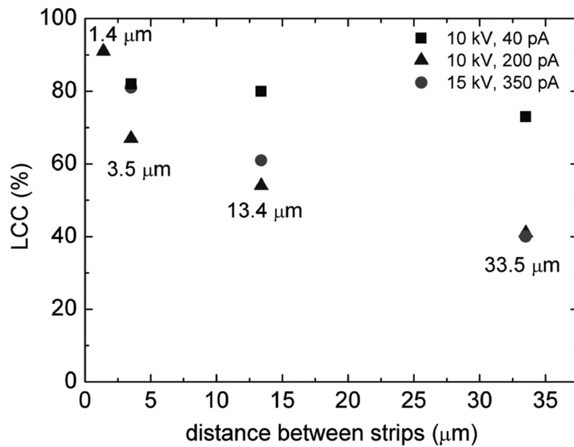

Fig. 8. *LCC* values versus the strip gap for different beam parameters with the n-i-p configuration and 10 μm intrinsic layer. For the 1.4 μm strip gap, results are available only for the 10 kV and 200 pA beam. Note that the error bars are smaller than the symbol size.

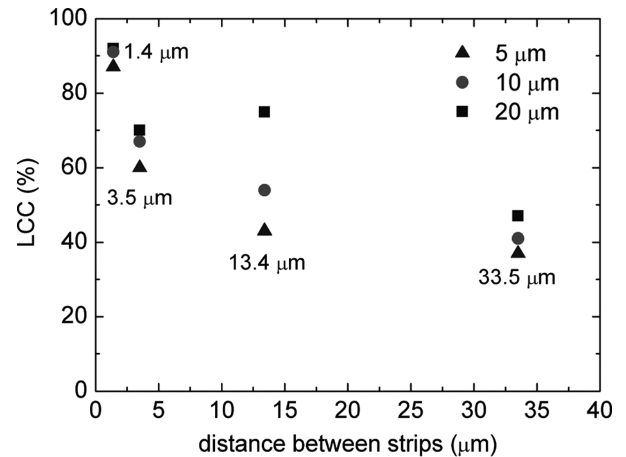

Fig. 9. *LCC* values versus the strip gap for different intrinsic layer thicknesses with the 10 keV and 200 pA beam. Note that the error bars are smaller than the symbol size.

D. Spatial Resolution for Different Beams

The *LCC* was used to compare the results obtained with different a-Si:H pixel configurations and electron beam energies.

Referring to Fig. 2, it is worth noting that the measured pixel configurations have all strips connected together so that the current between two strips results from the electrons collected by both of them. Consequently, for hypothetically independent strips, the *LCC* is expected to halve when the beam is between the two.

The *LCC* as a function of strip gap and beam characteristics is shown in Fig. 8 for the n-i-p diode configuration with an intrinsic layer 10 μm thick. The *LCC* decreases as a function of the strip gap, as expected, due to an increasingly larger voltage drop in the n-layer which weakens the electric field and hinders collection. The influence of the beam parameters on the *LCC* is clearly visible for all pixel configurations besides the one with 1.4 μm strip gap for which just one beam condition was measured. Table II shows that 10 keV and 200 pA are the optimal compromise in terms of lateral spread (compared to 15 keV) and density of generated charges (compared to 40 pA). This is confirmed by the experimental results of Fig. 8 for strips 3.5 and 13.4 μm apart. For gap widths of 13.4 and 33.5 μm, the lateral spread for any chosen beam energy remains smaller than half strip gap, which lets the *LCC* decrease for the 350 pA beam current as well. On the contrary, the 40 pA beam does not make the *LCC* drop significantly because the electric field weakening remains small due to fewer generated charges.

E. Spatial Resolution for Different Diode Thicknesses

The *LCC* dependency on different active layer thicknesses in the n-i-p configuration was also investigated and is shown in Fig. 9. We measured 5, 10 and 20 μm thick intrinsic layers with the 10 keV and 200 pA beam. The high TFA spatial resolution was confirmed even for the 20 μm layer and 1.4 μm strip gap with an *LCC* of $92\pm1\%$. The rather high *LCC* for strips 13.4 μm apart with a 20 μm intrinsic layer is explained by locally higher hillock concentration, which increased measurement noise and blurred the current modulation between strips. Otherwise, the *LCC* does not change much with intrinsic layer thickness and its small variations can be addressed to the same average electric field adopted for all samples discussed in Section IV-A. Indeed, upon creation of new defects during EBIC measurements, the electric field profile tends to vanish near the i/n interface and the electrons are assumed to diffuse to the n-layer with non-negligible lateral spread. Consequently, the voltage drop is less marked, which results in larger $I_{betstrips}$ and *LCC* for thicker intrinsic layers.

The overall induced current decreased by about 25% when the thickness increased from 5 to 20 μm. This effect could be an important limitation when working with even thicker active layers, which are required for high energy particle detection. Our group is currently tackling the problem by developing different a-Si:H diode architectures with more effective blocking contacts that hinder majority carrier injection and reduce the leakage currents. First promising results have been achieved by employing oxide layers [31], and their implementation in the TFA is in progress.

F. Spatial Resolution for Different Diode Configurations

We here compare the *LCC* for M-i-p and n-i-p diode configurations. The aim was to investigate the effects of the different collection path with electrons flowing laterally in the intrinsic layer (M-i-p) and in the n-doped layer (n-i-p).

The measurements were performed with a 20 keV and 350 pA beam on the 10 μm intrinsic layer for strips spaced by 3.5 and 33.5 μm. The *LCC* results are reported in Table III. Strips 33.5 μm apart exhibited the lowest *LCC* for the M-i-p configuration. This is explained by a weaker electric field in the beam interaction zone between strips, compared to the n-i-p configuration, due to the field lines converging towards the connected strips which increases charge recombination between strips.

Furthermore, for the 33.5 μm strip gap, the much lower *LCC* values of both the n-i-p and M-i-p configurations with respect to those presented in Figs. 8 and 9 can be explained by the larger a-Si:H degradation induced by the larger electron energy of 20 keV and a slower scan speed. Chronologically, these were the

TABLE III
LCC Values for M-i-p and n-i-p Configurations With the 10 μm Intrinsic Layer. The Electron Beam Parameters Were 20 keV and 350 pA

Configuration	Strip width (μm)	Strip gap (μm)	*LCC* (%)
M-i-p	16.5	33.5	7.4 ± 0.4
n-i-p	16.5	33.5	14.2 ± 0.8
M-i-p	1.5	3.5	80.6 ± 1.2
n-i-p	1.5	3.5	80 ± 1

first measurements, and the beam parameters were not yet optimized to limit the absorbed dose, which resulted in 17.6 MGy within 2250 $\mu\mathrm{m}^3$. As described in Section IV-B, this larger degradation caused both the current on strips and between strips to drop, whereas the leakage current increased. As a consequence, the *LCC* decreased to very low levels which were detrimental for precise beam position determination.

The *LCC* of the M-i-p and n-i-p configurations are comparable within the error bars for the 3.5 μm gap, and their high values are due to a large lateral spread of about 4 μm for the 20 keV electron beam.

G. Microvoids in a-Si:H Diodes

The micrometric spatial resolution presented so far was achieved with an a-Si:H intrinsic layer with microvoids, as we eventually observed. This was revealed in a cross section made by a focused ion beam (FIB) throughout the whole a-Si:H diode (10 μm thick) and the uppermost ASIC metallization layer, as shown in Fig. 10. Here, the FIB cut extends laterally from the pixel edge to the fifth connected 0.6 μm wide strip with 1.4 μm gaps. Each aluminum strip can be recognized as a brighter trapezoidal shape beneath the a-Si:H layer (inset of Fig. 10). Ditches due to the microstrip patterning, which extends below the aluminum metallization into the intermediate ASIC passivation layer, can be observed to be as deep as 2 μm. This rough surface caused the a-Si:H growing fronts from the lateral sides of the ditches to join, preventing conformal coating at the bottom of the ditch. These microvoids occurred even for the farthest apart strips (13.4 and 33.5 μm) due to the microstrip patterning technique used for these ASICs, which resulted in a very rough surface between strips. We assume that the microvoid edges are well passivated by the hydrogen present in a-Si:H and do not contribute much to recombination. However, these microvoids force charges to move laterally in the intrinsic layer, similar to what happens in the M-i-p configuration. For strips spaced by 3.5 μm, this effect can explain the similar *LCC* values for the M-i-p and n-i-p structures. Nevertheless, the overall effect of these microvoids does not significantly change the performance of the detectors (especially for the larger strip gaps of 13.4 and 33.5 μm), due to their shape, their position close to the back contact, and their small spatial extension, which is similar to a small vertical slit.

V. Conclusion

TFA were evaluated in terms of spatial resolution by employing a keV electron beam on pixels patterned in various microstrip geometries. The microstrips were connected to the

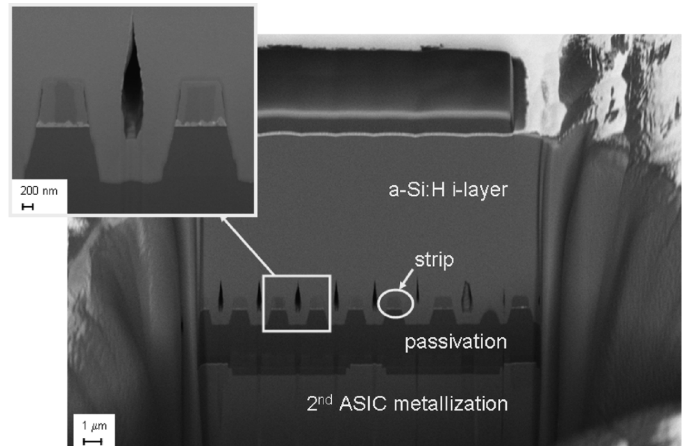

Fig. 10. Backscattered electron image of an FIB cross section throughout the 10 μm intrinsic layer plus the upper part of the ASIC showing the microstrip-patterned pixel, the intermediate passivation layer and the second metallization layer. In the inset, a detail of a microvoid between two strips 0.6 μm wide, spaced by 1.4 μm.

same front-end amplification circuit. Each microstrip signal was clearly distinguished in EBIC maps and individual beam sweeps, even for strips 0.6 μm wide spaced by 1.4 μm gaps, demonstrating the high spatial resolution of a-Si:H-based microstrip detectors. The current modulation which allowed us to determine the beam position and achieve high spatial resolution was induced by the weakened electric field across the diode and between two strips. This caused larger charge recombination and lower induced current with respect to the signal measured with the beam over the strips. Even better spatial resolution is expected for individually amplified strips.

These promising results were confirmed with three different active layer thicknesses of 5, 10 and 20 μm. The thicker the diodes, the slightly worse the spatial resolution due to the difficulty of keeping the active layer fully depleted during the measurements.

Two a-Si:H diode configurations were tested as well. For strips spaced by 33.5 μm gaps, the n-doped—intrinsic—p-doped (n-i-p) configuration is to be preferred because it exhibits smaller charge loss between strips than the metal—intrinsic—p-doped (M-i-p) one. On the contrary, strips with a 3.5 μm gap provided similar lateral charge collection and spatial resolution for both M-i-p and n-i-p structures, although M-i-p led to smaller leakage currents.

One major limitation for the TFA spatial resolution comes from the low energy electron beam used here with EBIC technique which produced a non-negligible lateral spread of the interaction volume. Better performances are expected for particle beams of higher energy and consequently lower lateral spread. The TFA is therefore well suited for particle beam diagnostic and tracking applications.

Finally, the high spatial resolution presented in this work was achieved despite the presence of microvoids at the bottom of the a-Si:H intrinsic layer. This emphasizes the potential of the TFA whose active layer can be deposited on front-end electronics with roughness as high as a few micrometers without major detrimental effects on spatial resolution.

Future work is envisaged on thicker detectors and limiting leakage currents. Tests with particle sources of higher energy and lower flux are also planned.

Acknowledgment

The authors would like to thank Dr. M. Dadras and Mrs. M. Leboeuf of the Centre Suisse d'Electronique et de Microtechnique (CSEM) of Neuchâtel for their help with the EBIC setup.

The authors would like to thank also Dr. D. Alexander for the FIB cross-section at the EPFL Centre Interdisciplinaire de Microscopie Electronique (CIME).

References

[1] S. Braibant *et al.*, "Investigation of design parameters for radiation hard silicon microstrip detectors," *Nucl. Instrum. Meth. Phys. Res. A*, vol. 485, pp. 343–361, 2002.

[2] N. Wermes, "Pixel detectors for tracking and their spin-off in imaging applications," *Nucl. Instrum. Meth. Phys. Res. A*, vol. 541, pp. 150–165, 2005.

[3] G. Rizzo, "Recent development on CMOS monolithic active pixel sensors," *Nucl. Instrum. Meth. Phys. Res. A*, vol. 576, pp. 103–108, 2007.

[4] P. J. Sellin and J. Vaitkus, "New materials for radiation hard semiconductor dectectors," *Nucl. Instrum. Meth. Phys. Res. A*, vol. 557, pp. 479–489, 2006.

[5] G. Pellegrini *et al.*, "Fabrication and simulation of novel ultra-thin 3D silicon detectors," *Nucl. Instrum. Meth. Phys. Res. A*, vol. 604, pp. 115–118, 2009.

[6] N. Wyrsch *et al.*, "Vertical integration of hydrogenated amorphous silicon devices on CMOS circuits," *Proc. Mater. Res. Soc.*, vol. 869, pp. 3–14, 2005.

[7] G. Anelli *et al.*, "A new concept of monolithic silicon pixel detectors: hydrogenated amorphous silicon on ASIC," *Nucl. Instrum. Meth. Phys. Res. A*, vol. 518, pp. 366–372, 2004.

[8] T. Lule, B. Schneider, and M. Böhm, "Sensitivity of CMOS based imagers and scaling perspectives," *IEEE Trans. Electron Devices*, vol. 47, pp. 2110–2122, 2000.

[9] J. Dubeau *et al.*, "Response of amorphous silicon p-i-n detectors to ionizing particles," *Nucl. Instrum. Meth. Phys. Res. B*, vol. 54, pp. 458–471, 1991.

[10] J. Dubeau, L. A. Hamel, and T. Pochet, "Radiation ionization energy in a-Si:H," *Phys. Rev. B*, vol. 53, pp. 10741–10750, 1996.

[11] M. Despeisse *et al.*, "Hydrogenated amorphous silicon sensor deposited on integrated circuit for radiation detection," *IEEE Trans. Nucl. Sci.*, vol. 55, pp. 802–811, 2008.

[12] S. N. Kaplan *et al.*, "Detection of minimum-ionizing particles in hydrogenated amorphous silicon," *Nucl. Instrum. Meth. Phys. Res. A*, vol. 273, pp. 611–614, 1988.

[13] W. S. Hong *et al.*, "Charged particle detectors based on high quality amorphous silicon deposited with hydrogen or helium dilution of silane," *IEEE Trans. Nucl. Sci.*, vol. 42, pp. 240–246, 1995.

[14] J. M. Marshall, R. A. Street, and M. J. Thompson, "Localized states in compensated a-Si:H," *Phys. Rev. B*, vol. 29, pp. 2331–2333, 1984.

[15] N. Wyrsch *et al.*, "Recent progress in the interpretation of a-Si:H transport properties: Lifetimes, mobilities and mobility-lifetime products," *Solid St. Phen.*, vol. 44–46, pp. 525–534, 1995.

[16] Q. Gu *et al.*, "Non-Gaussian transport measurements and the Einstein relation in amorphous silicon," *Phys. Rev. Lett.*, vol. 76, pp. 3196–3199, 1996.

[17] J. R. Srour *et al.*, "Damage mechanisms in radiation-tolerant amorphous silicon solar cells," *IEEE Trans. Nucl. Sci.*, vol. 45, pp. 2624–2631, 1998.

[18] N. Kishimoto *et al.*, "Radiation resistance of amorphous silicon in optoelectric properties under proton bombardment," *J. Nucl. Mater.*, vol. 258–263, pp. 1908–1913, 1998.

[19] N. Wyrsch *et al.*, "Radiation hardness of amorphous silicon particle sensors," *J. Non-Cryst. Solids*, vol. 352, pp. 1797–1800, 2006.

[20] U. Schneider, B. Schröder, and F. Finger, "The creation of metastable defects in a-Si:H films by high dose irradiation with keV-electrons," *J. Non-Cryst. Solids*, vol. 97 and 98, pp. 795–798, 1987.

[21] A. Yelon, H. Fritzsche, and H. M. Branz, "Electron beam creation of metastable defects in hydrogenated amorphous silicon: hydrogen collision model," *J. Non-Cryst. Solids*, vol. 266–269, pp. 437–443, 2000.

[22] A. Scholz, B. Schehr, and B. Schroeder, "Metastability in p- and n-type a-Si:H investigated by keV-electron irradiation," *Solid State Commun.*, vol. 85, pp. 753–757, 1993.

[23] G. Juška *et al.*, "Ultrafast charge carrier recombination in a-Si:H and μc-Si:H," *Phys. Stat. Sol.*, vol. 171, pp. 539–547, 1999.

[24] M. Despeisse *et al.*, "Characterization of 13 and 30 μm thick hydrogenated amorphous silicon diodes deposited over CMOS integrated circuits for particle detection application," *Nucl. Instrum. Meth. Phys. Res. A*, vol. 518, pp. 357–361, 2004.

[25] C. Miazza *et al.*, "Image sensors based on thin-film on CMOS technology: Additional leakage currents due to vertical integration of the a-Si:H diodes," *Proc. Mater. Res. Soc.*, vol. 910, pp. 409–414, 2007.

[26] G. Anelli *et al.*, "A high-speed low-noise transimpedance amplifier in a 0.25 mm CMOS technology," *Nucl. Instrum. Meth. Phys. Res. A*, vol. 512, pp. 117–128, 2003.

[27] D. Drouin *et al.*, "CASINO V2.42—A fast and easy-to-use modeling tool for scanning electron microscopy and microanalysis users," *Scanning*, vol. 29, pp. 92–101, 2007.

[28] H. J. Leamy, "Charge collection scanning electron microscopy," *J. Appl. Phys.*, vol. 53, no. 6, pp. R51–R80, 1982.

[29] S. Qureshi *et al.*, "Signal generation in a hydrogenated amorphous silicon detector," *IEEE Trans. Nucl. Sci.*, vol. 36, pp. 194–198, 1989.

[30] F. Meillaud *et al.*, "Efficiency limits for single-junction and tandem solar cells," *Sol. Energy Mater.*, vol. 90, pp. 2952–2959, 2006.

[31] M. Despeisse *et al.*, "Resistive interlayer for improved performance of thin film silicon solar cells on highly textured substrate," *Appl. Phys. Lett.*, vol. 96, p. 073507, 2010.